Experimental Demonstrations of High-Accuracy 3D/2D Indoor Visible Light Positioning Using Imaging MIMO Receivers and Artificial Neural Networks

Apolo, Juan A.; Osahon, Isaac N. O. ; Ortega, Beatriz; Tang, Jianming; Rajbhandari, Sujan

IET Optoelectronics

DOI:
10.1049/ote2.70000

Published: 07/02/2025

Peer reviewed version

Experimental Demonstrations of High-Accuracy 3D/2D Indoor Visible Light Positioning Using Imaging MIMO Receivers and Artificial Neural Networks

Juan. A. Apolo[1*], Isaac. N. O. Osahon[2], Beatriz Ortega[1], Vicenç Almenar[1], Jianming Tang[3] and Sujan Rajbhandari[4]

[1]Instituto de Telecomunicaciones y Aplicaciones Multimedia, ITEAM, Universitat Politècnica de València, Valencia 46022, Spain
[2]Electrical Engineering Division, University of Cambridge, Cambridge CB3 0FA, UK
[3]DSP Centre of Excellence, School of Computer Science and Electronic Engineering, Bangor University, Bangor LL57 1UT, UK
[4]Institute of Photonics, Department of Physics, University of Strathclyde, Technology & Innovation Centre, Glasgow G1 1RD, UK
[*]juaapgon@teleco.upv.es

Abstract: This paper proposes and presents the first experimental demonstration of a high-precision indoor 2D and 3D visible light positioning (VLP) system using an imaging multiple-input multiple-output (MIMO) configuration with supervised artificial neural network (ANN). The proposed system utilizes four distributed transmitters and receivers with four photodiodes and an imaging optics. The experiments are conducted in a typical indoor environment with transmitter separations of 300 mm and a link distance of 1400 mm. The experimental results show 2D and 3D positioning accuracies of 3.7 mm and 51 mm, respectively. A simulation model is also developed for the VLP system to verify the experimental results. Further optimization of the VLP system in the simulation platform leads to improved 2D and 3D positioning accuracies of 2 mm and 9.3 mm, respectively. The proposed system can seamlessly converge with existing lighting infrastructures and is also compatible with the imaging MIMO visible light communication (VLC) system, indicating the potential for practical implementation in integrated communications and positioning applications.

1. Introduction

Over the past decade, visible light communication (VLC) has emerged as a complementary technology to traditional radio frequency (RF)-based wireless communications. VLC leverages existing solid-state lighting infrastructure for high-speed wireless communication, thus offering advantages such as unlicensed spectrum operation, low power consumption, and reduced implementation costs [1]. Operating in the unlicensed spectrum while still maintaining low power consumption, this technology is expected to play a key role in upcoming 6G networks, demonstrating high-speed transmission capabilities and compatibility with various communication systems. In addition, it also offers an alternative for integrating aerial, submarine, and indoor networks for 6G and beyond [2]. Among its many applications, indoor and outdoor visible light positioning and navigation are promising areas.

Positioning technologies have recently attracted significant attention due to their applications in wide-ranging monitoring, surveillance, or tracking. Compared to RF positioning technologies, visible light positioning (VLP) offers unique advantages of high-accuracy due to shorter wavelengths and less sensitivity to multipath propagation, zero electromagnetic interference (EMI), and dual functionalities of illumination and positioning [1].

VLP systems utilize photodiodes (PDs) or image sensors (IS) receivers to provide indoor positioning solutions. PD-based VLP systems offer advantages such as fast response times, compatibility with communications, and suitability for real-time applications and varying lighting conditions. Existing PD-based VLP techniques can be classified into two main categories: distance-based and distance-free [3], [4]. Distance-based techniques include the use of received signal strength (RSS) to estimate the distance between the receiver (Rx) and the transmitter (Tx) [5]. Other distance-based techniques employ time of arrival (TOA) [6] and time difference of arrival (TDOA) [7]; both require precise synchronization between transmitters and receivers, resulting in increased system complexity. Furthermore, angle of arrival (AOA) based techniques require diversified angles and a relatively large number of receiver devices to operate effectively [8]. Distance-free techniques are independent of geometric distance measurements, but often require more complex hardware and configuration. One commonly adopted distance-free technique uses RSS values as fingerprint features for indoor positioning [9].

In contrast to PD-based VLP systems, IS-based VLP systems capture the images of the modulated intensity of LED luminaires and subsequently process them using image processing algorithms to estimate the position [10]. This enables the extraction of detailed features, the improvement in interference rejection, and the elimination of multipath reflections [11]. Furthermore, cameras are extensively incorporated into consumer devices, such as smartphones, enabling VLP systems to use existing hardware. However, these systems are subject to several challenges, including

Table 1: Key experimental parameters for imaging VLP system overview of diversity receiver based VLP systems and original contribution of proposed work.

Reference/year	Technique	Type of Study	Number of Txs	Number of PDs	Room dimensions (mm) L×W×H	3D	Compatible with communications	Accuracy
[17], 2018	RSS	Simulation	1	4	3000×3000×1250	No	No	35.0 mm @ 90% CDF
[18], 2021	RSS fingerprinting with fabricated data and ML	Experimental	4	4	1200×1200×1600	No	No	8.3 mm @ 90% CDF
[19], 2022	AOA with LSTMNN	Experimental	1	4	400×400	No	No	29.0 mm @90% CDF
[20], 2018	Three different ANNs (one for each axis)	Simulation	16	361 (19 ×19)	4000×4000×3000	Yes	No	0.4 mm @90% CDF
[21], 2022	RSS fingerprinting (ML) ANN	Simulation	4	1-4	5000×5000×5000	Yes	No	19.8 mm @ 90% CDF (LOS-3D) 10.3 mm @ 90% CDF (LOS-2D)
[22], 2024	Deep residual shrinkage network (DRSN)	Experimental & Simulation	1	4	3600×3600×3000	Yes	No	23.5 mm @90% CDF (Simulation) 100 mm @90% CDF (Experimental)
Our work	RSS fingerprinting MLP-ANN with Imaging receiver	Experimental & Simulation	4	4	400×400×120	Yes	Yes	2 mm (2D) @90% CDF 9 mm (3D) @90% CDF

slower response times generally unsuitable for high-speed communication due to their limited frame rates and sensitivity to lighting conditions, which can affect the accuracy and difficulty of employing them in real-time systems, which limits their effectiveness in specific scenarios.

Advanced solutions for accurate VLP have been proposed based on machine learning and deep learning (ML/DL), i.e., linear or higher-order regression [12]. Various algorithms, such as K-nearest neighbor (KNN), support vector machine (SVM), and artificial neural network (ANN) [13], are showcasing promising outcomes and achieving mm levels of accuracy, thereby offering potential solutions for VLP. These techniques are often used in fingerprint-based systems, where a database of RSS values and their corresponding coordinates is pre-collected. ANNs, for instance, are trained using the offline fingerprint data. Once trained, ANNs can accurately predict a user's location in real-time based on new RSS measurements. The Multi-Layer Perceptron (MLP) network, often configured with a single hidden layer, is a commonly chosen ANN architecture for conducting localization tasks [14], [15].

The spatial diversity provided by multiple PDs improves the robustness of the positioning system against obstacles and interference, which are common factors in indoor environments [16]. Moreover, the literature shows the use of multiple PDs in experimental VLP systems to improve positioning accuracy, as detailed in Table I. For example, tilted PDs were proposed to improve the accuracy of VLP systems [17], where a localization error of 35 mm was obtained. Furthermore, a ML technique is combined with multiple detectors to provide higher accuracy. In [18], four PDs and RSS-based fingerprinting with a Weighted K-nearest neighbors (WkNN) algorithm were employed to demonstrate positioning errors of 8.3 mm and 20.45 mm with four and two luminaires, respectively. A VLP system based on a single LED and multiple silicon solar cells employing AOA and a long short-term memory neural network (LSTMNN) model has achieved an average positioning error of 17.8 mm, and 90% of the experimental data had a positioning error within ~29 mm [19]. A theoretical approach based on 16 LED lamps and a grid of 361 receivers with three ANNs to estimate 3D positioning from RSS has achieved an average distance error of 0.4 mm [20]. In [21], the authors proposed a VLP system based on four evenly distributed LED emitters and a MLP for 2D positioning with an estimation of the root-mean-square (RMS) errors as 10.3 mm and 13.3 mm for LOS and non-LOS links, and 19.8 mm and 21 mm for 3D localization. In [22], the authors propose a deep residual shrinkage network (DRSN) with a single LED and 4-PDs. The system achieves an accuracy where 90% of the errors are below 23.5 mm in simulations and below 100 mm in experiments.

The LiFi-based integrated communication and positioning paradigm is expected to be a key technology for 6G networks [23]. In VLC/LiFi technologies, numerous studies have shown high-speed communications utilizing multiple-input multiple-output (MIMO) configurations and accurate VLP positioning facilitated by a distributed illumination infrastructure [24]. The optical MIMO receiver can be realized using imaging and non-imaging configurations [25]. Imaging MIMO systems are preferred over non-imaging MIMO configurations due to enhanced data rate scalability, compactness, and a well-conditioned channel H-matrix [25], [26]. However, to the best of the authors' knowledge, there has been no previously published work demonstrating imaging MIMO configurations for highly accurate VLP. This paper is the first attempt to showcase highly accurate 2D/3D VLP using imaging MIMO setups. While this paper primarily focuses on proof-of-concept demonstrations of VLP using such configurations, the overarching objective is to exhibit integrated communications and positioning in future iterations.

Hence, the novelty and original contributions of this paper are as follows:

- To the best of the authors' knowledge, this is the first experimental demonstration and simulation study of imaging optical MIMO configuration for 2D/3D positioning. Furthermore, this is the first study of utilizing the supervised ANN with imaging MIMO for VLP.

- This paper provides a comprehensive study of the impact of defocusing the lens position in the receiver on VLP performance; clearly demonstrating the trade-off between the field of view (FOV) and positioning accuracy
- This is the first experimental demonstration to verify the improved 2D and 3D positioning accuracy due to imaging spatial diversity provided by multiple PDs.
- This work demonstrates the potential of imaging MIMO VLP configuration for integrated sensing and communication applications, aligning with future 6G network requirements.

The subsequent sections of this work are organized as follows: section 2 provides a detailed description of the proposed VLC positioning system, including the experimental setup and the signal processing for the ANN algorithm. Section 3 presents the results obtained from both laboratory measurements and simulations evaluating the accuracy of the 2D/3D positioning system. Finally, section 4 presents the conclusions of this work by summarizing the feasibility and accuracy of the proposed 2D/3D VLP system and identifying the main challenges for further research.

2. System description and experimental setup

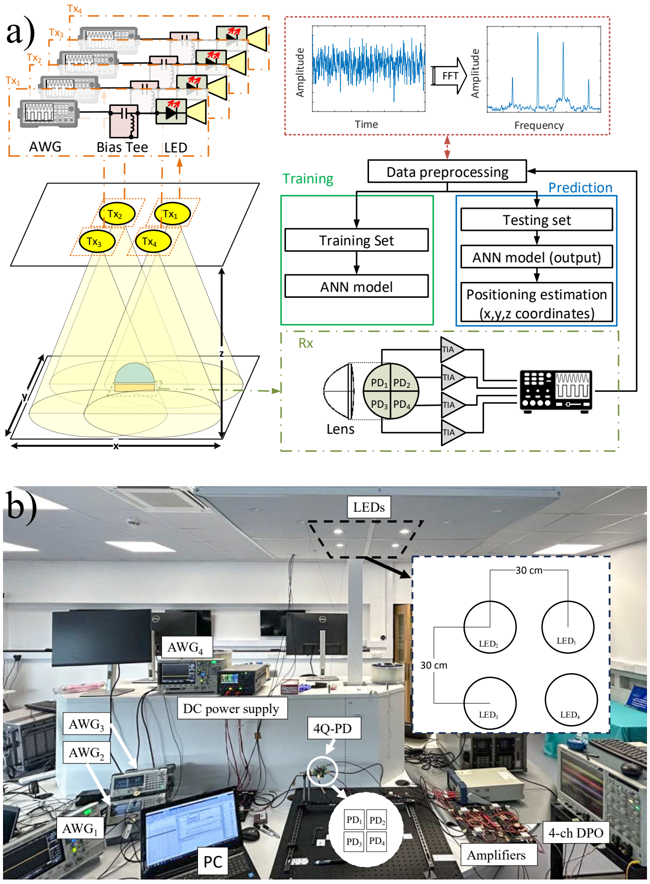

Fig. 1. Multi-PD VLP system with an imaging receiver: (a) Schematic diagram; (b) Photograph of the laboratory setup. The insets show the geometrical distribution of the transmitters and receivers.

Fig. 1(a) depicts the experimental setup of the VLP system proposed in this work, including the Tx and Rx configurations, the signal processing procedure at the Rx, and position estimation based on ANN, which will be described in detail in this section. The experimental parameters are summarized in Table II. The proposed VLP system employs a 4 × 4 imaging MIMO configuration that utilizes white LEDs as Txs and an imaging receiver with a PD array as Rx, in a similar arrangement to other MIMO-VLC imaging systems [27], [28].

2.1. Transmitter

The VLP system utilizes four symmetrically distributed Txs, spaced 300 mm apart, serving as illumination sources and signal transmitters for position estimation. Each transmitter comprises an LED (Samsung LM561C) and a reflector (LEDiL EMILY-W), producing a 40° beam divergence. The LED operates with an average bias current of 75 mA, creating a luminous flux of 46 lumens. Modulating signals are generated by four arbitrary waveform generators (AWGs), whose outputs are converted into unipolar signals adding DC voltages using bias-Tees (MINI-CIRCUITS, ZFBT-4R2GW-FT+). Thus, a non-negative amplitude of the signal is ensured to modulate the intensity of each LED. Since the distance between the ceiling and the detector plane in the 2D VLP configuration is fixed at 1400 mm, the 40° divergence gives rise to a circular coverage area of approximately 817 mm^2 (510 mm radius) for each transmitter.

2.2. Receiver

Our imaging MIMO VLP configuration employs a plano-convex aspheric singlet lens (THORLABS, ACL2520U) with a 25 mm diameter and a 20.1 mm focal length as the imaging optics. A PD array with four independent elements is used as the receiver, as shown in Fig. 1. As stated in [29], the FoV can be improved by defocusing (i.e., placing receivers at the offset distance (f_{offset}) towards the lens from the focal plane) instead of placing the receiver at the focal plane. Then, the receiver can achieve a wider FoV to support improved localization while maintaining a sufficient signal-to-noise ratio (SNR) for reliable positioning operation. Hence, we utilized the focal offset (f_{offset}) of 4 mm, providing a FoV of 37.5°, which closely matches the transmitter beam divergence of 40°. The signal output from each PD is independently amplified by a trans-impedance amplifier (TIA) (MAX3665) followed by a low-noise amplifier (LNA) with a 20-dB gain (MINI-CIRCUITS, ZFL-1000LN+). A 4-channel digital oscilloscope captures the signal, with each channel corresponding to each amplified PD output, followed by offline processing. The maximum SNR in our setup is measured as 51.9 dB.

Table 2: Key experimental parameters for imaging VLP system.

	Parameter	Value
LED	SAMSUNG LM561C	
	Bias current I_b	75 mA
	Bias voltage V_{DC}	3.3 V
	Flux	43 lm @75 mA
Reflector	LEDiL CA11934_EMILY-W	
	External diameter	Ø 26 mm

	Parameter	Value
	FWHM	40°
RX lens	Thorlabs ACL2520U-A	
	Diameter	Ø25 mm
	Focal Length f_c	20.1 mm
	Back Focal Length f_b	12mm
PD	First Sensor QP5.8-6-TO5	
	Number of elements	4
	Active area of each PD	1.44 mm^2
	Responsivity	0.4 A/W @632 nm
	Element gap	50 µm
Amplifier	Mini-Circuits ZFL-1000LN+	
	Gain	19.9 dB
	Noise Figure	2.9 dB
General		
	Discrete frequencies	200, 400, 600, 800 kHz
	No. of transmitters, M_{Tx}	4
	No. of receivers, N_{Rx}	4
	Test Area	3D 540 × 540 × 120 mm^3
		2D 410 × 410 m^2

2.3. VLP channel

For the MIMO configuration with N_{Tx} transmitters and M_{Rx} receivers, the received signal can be calculated as:

$$\mathbf{S} = \mathbf{HX} + \mathbf{n}; \tag{1}$$

where $\mathbf{H}$ is the $N_{Tx} \times M_{Rx}$ channel matrix; $\mathbf{X}$ is the $N_{Tx} \times 1$ transmitted signal vector; $\mathbf{n}$ is the $M_{Rx} \times 1$ noise vector and $\mathbf{S}$ is the $M_{Rx} \times 1$ received signal vector. Note that for the imaging optical MIMO communication system, $M_{Rx} \geq N_{Tx}$. However, such a requirement is not necessary for the VLP-only applic_ations, though a higher number of Rx improves the positioning accuracy, as detailed in Section III. The channel gain from each Tx to each Rx, known as the channel $\mathbf{H}$-matrix, is given by:

$$\mathbf{H} = \begin{bmatrix} h_{11} & h_{12} & \cdots & h_{1N_{Tx}} \\ h_{21} & h_{22} & \cdots & h_{2N_{Tx}} \\ \vdots & \vdots & \ddots & \vdots \\ h_{M_{Rx}1} & h_{M_{Rx}2} & \cdots & h_{M_{Rx}N_{Tx}} \end{bmatrix}; \tag{2}$$

where h_{ij} is the channel gain from the j^{th} transmitter to the i^{th} receiver element. The channel gain information is related to RSS and can be used for positioning estimation.

For simplicity, we have employed frequency division multiplexing (FDM) with four discrete frequencies to distinguish the signals from individual LEDs instead of time division multiplexing (TDM), where a low-frequency sinusoid signal is transmitted in time sequence from each transmitter [27]. The Fast Fourier Transform (FFT) is applied to the received signal to compute the RSS corresponding to each transmitter. This operation is necessary to separate the FDM signals from multiple transmitters and prepare the inputs to the ANN for further processing.

2.4. Artificial Neural Network model

As shown in Fig. 2, a fully connected feedforward backpropagation supervised multi-layer perceptron (MLP) ANN with one input layer, one hidden layer, and one output layer is implemented for 2D/3D positioning estimation. The number of neurons in the input layer equals $M_{Rx} \times N_{Tx}$ corresponding to the channel $\mathbf{H}$-matrix for a particular position in (2). The output layer has a linear transfer function with two/three neurons corresponding to 2D/3D positioning, respectively. A detailed description of the ANN structure and corresponding training algorithm, including the optimization process for the hidden layer, can be found in [21]. Based on the optimization, the hidden layer has 32 neurons with a sigmoid transfer function. The sigmoid transfer function is selected for its capacity to introduce non-linearities into the model, enabling the network to learn from the training data. A dataset containing different RSS matrices paired with their corresponding positions is used to train the ANN, which jointly represents the spatial distribution of RSS. During training, the network adjusts its weights to minimize errors between the estimated and actual positions. This is achieved by backpropagation, where the error gradient is propagated backward through the network, allowing the optimization of the neural network parameters [30]. While various algorithms can be used with backpropagation to update the weights and biases of the MLP-ANN, we specifically use the Levenberg-Marquardt algorithm due to its superior convergence speed and minimal epoch requirements compared to alternative methods [31].

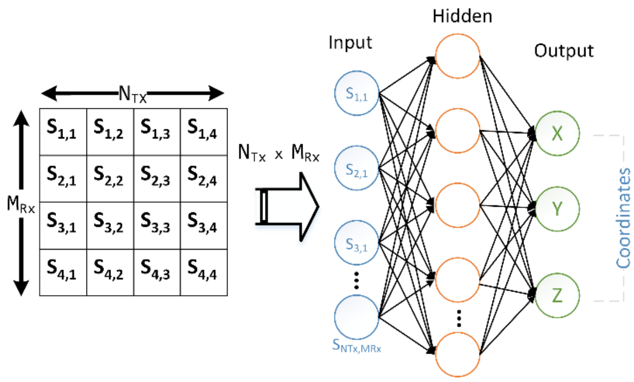

Fig. 2. Schematic diagram of ANN model for VLP.

3. Results and Discussion

3.1. Experimental results

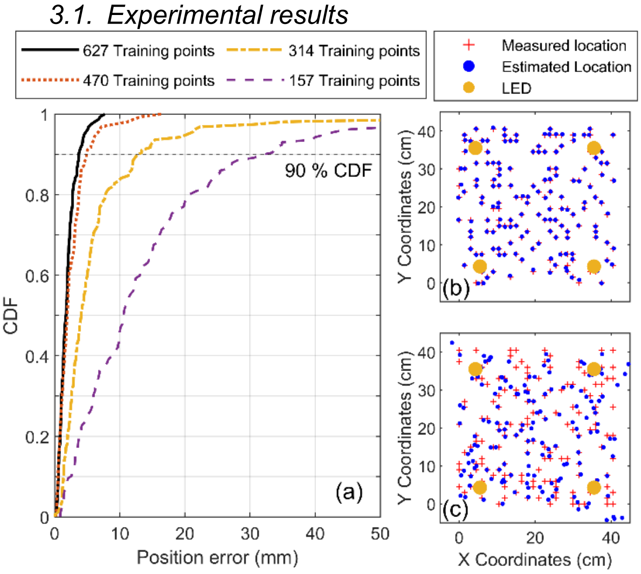

Fig. 3. (a) CDF of geometrical error of the proposed 2D VLP system using different numbers of training points. Location of the measured and estimated points by the ANN algorithm using different numbers of points: (b) 627 and (c) 157.

The experiment aimed to evaluate the accuracy of the proposed 2D/3D positioning system by conducting measurements within the predefined areas. A grid of 2D points with a geometric spacing of 15 mm was created to evaluate the positioning accuracy. Hence, by measurements, we collected 784 points within a 410 × 410 mm^2 area. This geometric spacing was chosen to balance a detailed spatial analysis with the practical constraints of measurement time. The system was evaluated based on the geometrical error's cumulative distribution function (CDF). Unless otherwise specified, we will use a CDF of 0.9 to specify the positioning error throughout the paper.

Fig. 3(a) shows the empirical CDF of the positioning error for different numbers of ANN training data. Training ANN with 80% of the dataset (627 points) resulted in a positioning error of 3.7 mm. Conversely, reducing the number of training data to 60%, 40%, and 20% of the dataset led to performance degradations and increased positioning errors of 4.9 mm, 12.6 mm, and 31.6 mm, respectively. Figs. 3(b) and (c) present the spatial distributions of errors across the test area. The figures compare the actual locations (denoted by crosses) with the locations estimated by the proposed system (represented by points). In Fig. 3(b), 627 training points were employed, and a smaller spread of the estimated positions around the actual positions is observed, indicating a higher overall positioning accuracy. In comparison, Fig. 3(c) shows the results when 157 training points were used, representing 20% of the dataset. This figure shows a sparser distribution of estimated positions, reflecting the degradation in system performance due to the smaller training dataset size.

To assess the 3D positioning accuracy, measurements were conducted within a 540 × 540 × 120 mm³ space. The grid is structured by points spaced 30 mm apart, with 361 points for each 2D plane and five different vertical levels, i.e., five 2D planes spaced 30 mm apart. The dataset comprises 1805 measurement points, 80% of which were used to train the ANN, and the remaining 20% were used to test and validate the algorithm.

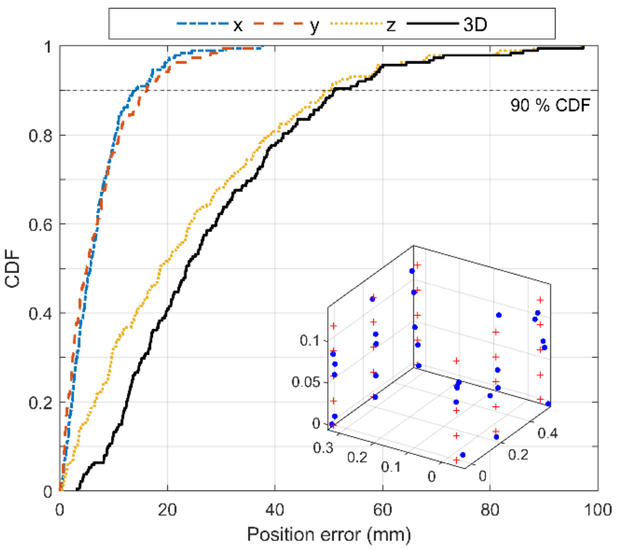

Fig. 4. CDF of geometrical error of the proposed 3D VLP system, including the detail of individual *x*-, *y*-, and *z*- plane in the 3D positioning. The inset shows the 3D scatter plot of the test and estimated positioning points.

Fig. 4 shows the geometric error in the *x*-, *y*- and *z*-planes. The positioning accuracies in the *x*- and *y*-planes are comparable, where the error is close to 15 mm. As expected, the accuracy in *x*- and *y*-planes is similar to the value in 2D positioning experiments presented in Fig. 3 for a similar number of training points (314). In contrast, the *z*-plane has a significantly higher error of ~51 mm. This difference in error between the dimensions is due to the reduced number of training points in the *z*-plane, which results in lower positioning accuracy. The inset in Fig. 4 visually compares 30 test points (crosses) and the estimated positions (dots) in that plane.

Fig. 5 demonstrates the impact of the receiver diversity on the accuracy of 2D and 3D positioning. In the case of 2D positioning, the positioning errors are 30 mm, 6 mm, 5 mm, and 3.7 mm for one, two, three, and four PDs, respectively (see Fig. 5(a)). Similarly, Fig. 5(b) shows that the 3D positioning errors are 78 mm, 61 mm, 60 mm, and 51 mm for one, two, three, and four PDs, respectively. This clearly illustrates the advantage of a PD array receiver system with imaging optics in enhancing positioning accuracy. We anticipate further enhancements in 3D positioning by increasing the number of training points along the *z*-plane, as shown in the following section.

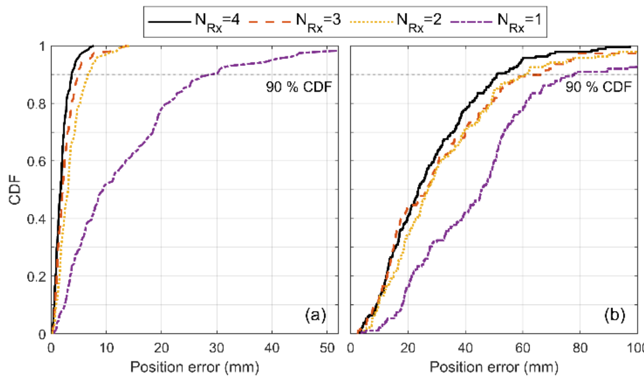

Fig. 5. CDF of geometrical error of the proposed VLP system with different diversity order N_{Rx} = 1-4 for: (a) 2D VLP and (b) 3D VLP.

3.2. Simulation results

The ZEMAX OpticStudio software is employed to verify and further extend the experimental results. The simulation scenarios replicate the experimental configurations and components described in the previous section, while optical powers and shot noise are adjusted to match the laboratory measurement conditions. For 2D positioning, simulations were conducted in a 410 × 410 mm^2 area using the same grid and number of points as in the experiment. However, the imaging optics system was optimized by varying f_{offset}, i.e., distance of the lens from its focal point towards the detectors to modify the size of the image formed at the receiver, to study the impact on positioning accuracy.

Fig. 6(a) presents the CDF of the positioning error of the 2D-VLP system for f_{offset} ranging from 0 to 6 mm. As in the case of experimental work, 80% of the dataset is used to train the ANN, and the remaining 20% is used for testing. The solid line represents the CDF obtained from laboratory measurements, showing excellent agreement with simulation results, with a positioning error of 3.7 mm at f_{offset} = 4 mm.

This correspondence validates the accuracy of the simulation model in replicating the experimental setup, allowing further extension of the experimental findings. The positioning error initially decreases with increasing f_{offset}, reaching a minimum error of approximately 2.6 mm at f_{offset} = 2 mm; beyond this point, the error begins to increase. For instance, the positioning errors for f_{offset} of 3 mm and 4 mm are ~2.9 mm and 3.5 mm, respectively.

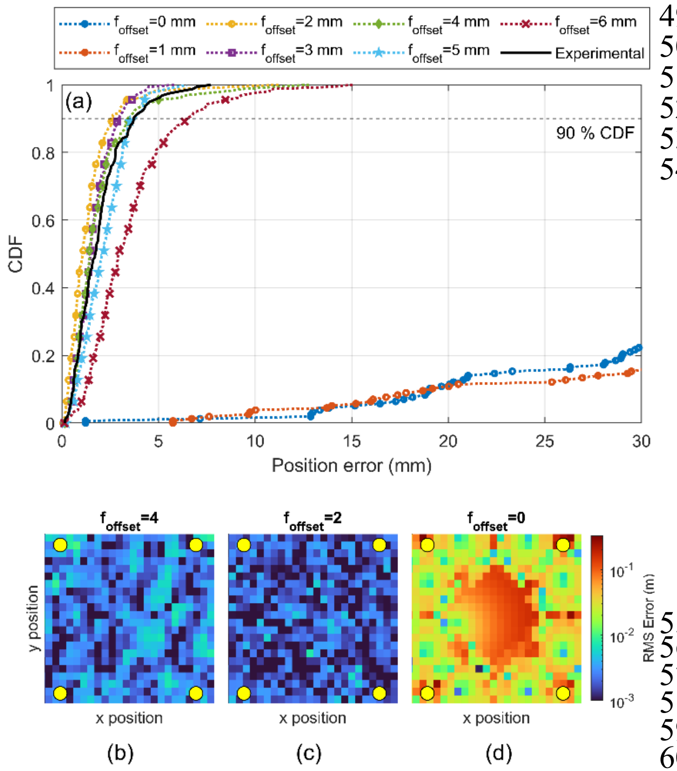

Fig. 6. (a) CDF of geometrical error from simulations for different focal offsets between the lens and the photodetectors (black curve corresponds to experimental results). Spatial distribution of the geometrical error for: (b) f_{offset} = 4 mm (c) f_{offset} = 2 mm and (d) f_{offset} = 0 mm. The yellow circles represent the location of the four transmitters.

Figs. 6(b), (c), and (d) show the spatial distributions of the geometric error for an offset of 4 mm, 2 mm, and 0 mm, respectively. Figs. 6(b) and (c) reveal a relatively uniform distribution of positioning errors across the measured area. In contrast, Fig. 6(d) corresponding to f_{offset} = 0 mm shows a notable variation in error distribution, with certain regions exhibiting significantly higher errors, particularly in the center. These areas of increased error are due to lower received signal intensity, as the image of Tx does not fall into any of the PDs due to narrow FoV (discussed further below).

Fig. 7 provides a further analysis of the imaging MIMO VLP system. The simulation of the spatial intensity distribution (incoherent irradiance W/m^2) depicts the received optical intensity at the image plane. The red lines represent the PD array in the image plane. The first row (Figs. 7(a), (b), (c)) depicts the images formed when the detector is located at the geometrical center formed by the transmitters. The second row (Figs. 7(d), (e), (f)) represents the images formed when the receiver is positioned directly below one of the transmitters. Each column represents a f_{offset} of 4 mm, 2 mm and 0 mm (from left to right). As observed, the focal offset significantly impacts the spatial distribution of intensity. The clearest image is formed when the receiver plane is at the focal point (f_{offset} = 0 mm). However, the images from the transmitters are outside the PDs, significantly reducing the received power. On the other hand, at f_{offset} = 4 mm, the images formed from the transmitters overlap significantly and are difficult to distinguish (this overlap leads to substantial inter-channel interference, resulting in a higher condition number for the MIMO **H**-matrix). In contrast, f_{offset} = 2 mm proves to be the optimal configuration, showing a clearly separated image from the four transmitters. Hence, as in the case of the imaging MIMO-VLC system [31], the condition number of channel **H**-matrix affected the positioning accuracy, and optimization of the optic system is necessary to obtain the best condition number.

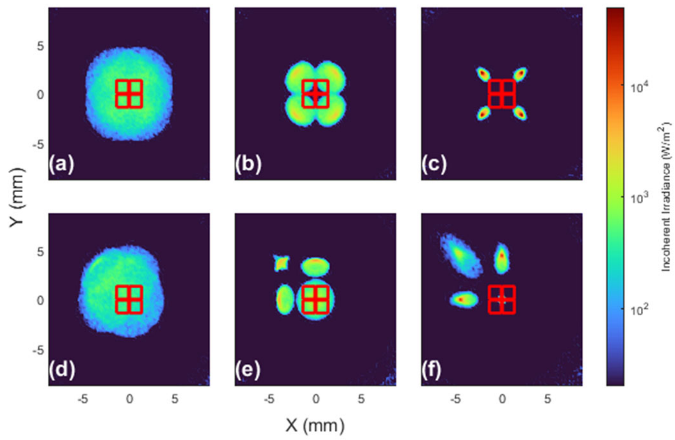

Fig. 7. Simulation of the image formed by the transmitters at the detector plane for different f_{offset} and different locations. First row: The receiver is at the geometric center of the four transmitters and f_{offset} is: (a) 4 mm, (b) 2 mm, and (c) 0 mm. Second row: The receiver is located directly under one of the transmitters and f_{offset} is: (d) 4 mm, (e) 2 mm, and (f) 0 mm. The red lines represent the PD array of four elements at the imaging plane.

Furthermore, the impact of SNR on the VLP performance is shown in Fig. 8, where the position accuracy has been estimated for the best-case configuration f_{offset} = 2 mm under an SNR range of 25–60 dB. As expected, the accuracy of the system decreases as the SNR decreases. In particular, the accuracy decreases from ~2 mm to ~16.9 mm when the maximum SNR reduces from 60.9 dB to 25.9 dB. However, the SNR has only a marginal impact on the positioning at high SNR, e.g., position accuracy decreases from 2 mm to 2.4 mm when SNRs are 60.9 dB and 50.9 dB, respectively. The insets illustrate the SNR distribution over the measurement area for a single transmitter and a single PD from the array. Note the significant drops in SNRs towards the edge of coverage areas.

Finally, simulations for both 2D and 3D positioning were carried out in an enlarged area of 600 × 600 × 240 mm^3 under the same configuration as employed in the laboratory (f_{offset} = 4 mm) for estimating the potential accuracy of the experimental 3D positioning system with a larger number of dataset points. The simulation grid is structured by points spaced 15 mm apart in the horizontal and vertical dimensions. This configuration results in a total of 1681 points in each of the 2D planes. The grid was divided vertically into 17 different levels (±120 mm from the 2D level); thus, the simulation dataset comprises 28577 points for 3D. As in all other cases, 80 % of the dataset (22861) is used to train the

ANN, and the remaining 20% is used for testing (5715). Fig. 9 displays the CDF of the 3D positioning along the *x*-, *y*- and *z*-planes, as well as the combined total positioning error.

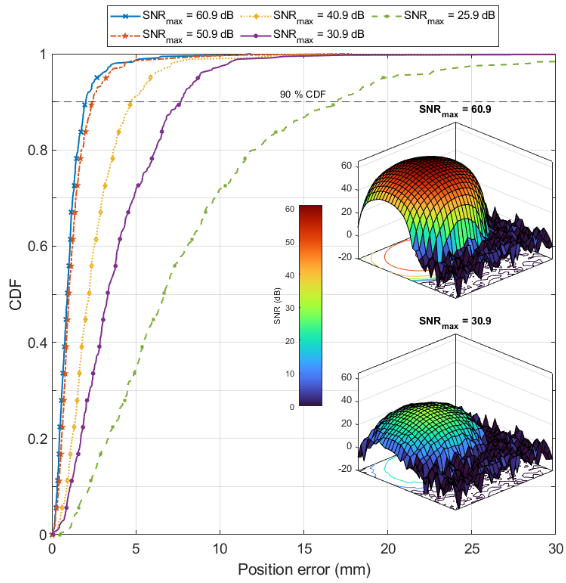

Fig. 8. CDF of the geometric error from simulations with a configuration of f_{offset} = 2 mm and 1513 dataset points for different SNR = 60.9–25.9 dB. Insets show the SNR distribution within the measurement area for one LED and one PD from the array for the best-case scenario of: (i) 60.9 dBm and (ii) 30.9 dBm.

The *x*- and *y*-planes errors are similar and relatively low, with positioning errors of ~6.9 mm. The *z*-plane, on the other hand, exhibits a greater error of 15.0 mm. The total 3D positioning error, which combines the errors of all three axes, is 16.8 mm, which is significantly lower than the experimental results of 51 mm. This improvement is due to the higher density of training points in the *z*-plane in the simulation, which allows for a more accurate representation of the measurement space and shows the potential of our approach for further improvement under larger training schemes.

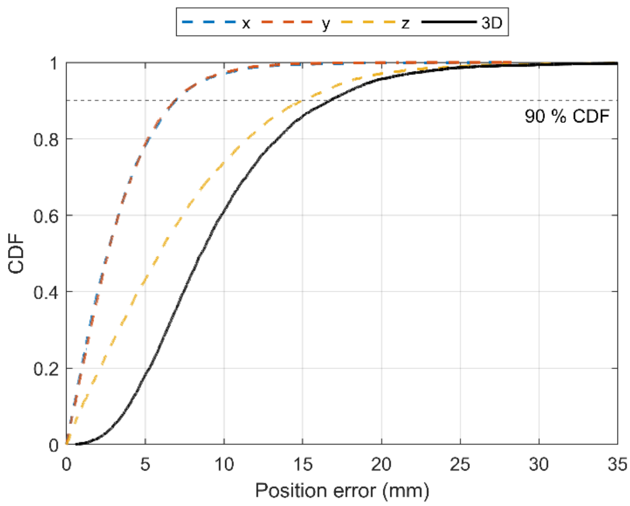

Fig. 9 CDF of geometrical error for 3D VLP from simulations with a configuration of f_{offset} = 4 mm and 28577 dataset points.

4. Conclusions

This paper presents an experimental demonstration of a high-accuracy 2D and 3D VLP system using an optical imaging MIMO system with supervised ANN. Experimental results show the impact of the number of training points and the spatial diversity on positioning accuracy, leading to 3.7 mm and 51 mm for 2D and 3D positioning accuracy, respectively.

The experimental work is validated and further extended by simulations. The simulation results allow to estimate the required number of training points and evaluate the impact of the system noise. Furthermore, the study underscores the critical role of optimizing the imaging optics, particularly the focal offset, in achieving high-accuracy positioning. Using the experimental parameters under an optimized system configuration, the simulations demonstrated a minimum positioning error of 2.0 mm and 9.3 mm for 2D and 3D positioning, respectively. Therefore, high-accuracy 2D/3D positioning has been demonstrated in a scalable imaging MIMO configuration as a promising solution for integrated positioning and communications applications. These advantages lead the proposed VLP imaging MIMO system as a promising solution for future 6G networks requiring high-precision indoor positioning capabilities.

5. Acknowledgment

This work has been supported by COST action CA19111 (NEWFOCUS). It has also been funded by Grant PID2021-126514OB-I00 OPTIMIZE by MCIN/AEI/ 10.13039/501100011033 and ERDF “A way of making Europe”. SR and JT acknowledge support by the UK Engineering and Physical Sciences Research Council under Grant EP/Y037243/1 (TITAN Extension).

6. References

[1] P. Chen, M. Pang, D. Che, Y. Yin, D. Hu, and S. Gao, ‘A Survey on Visible Light Positioning from Software Algorithms to Hardware’, *Wireless Communications and Mobile Computing*, vol. 2021, no. 1, p. 9739577, Jan. 2021, doi: 10.1155/2021/9739577.

[2] N. Chi, Y. Zhou, Y. Wei, and F. Hu, ‘Visible Light Communication in 6G: Advances, Challenges, and Prospects’, *IEEE Vehicular Technology Magazine*, vol. 15, no. 4, pp. 93–102, Dec. 2020, doi: 10.1109/MVT.2020.3017153.

[3] H. Q. Tran and C. Ha, ‘Machine learning in indoor visible light positioning systems: A review’, *Neurocomputing*, vol. 491, pp. 117–131, Jun. 2022, doi: 10.1016/j.neucom.2021.10.123.

[4] J. Luo, L. Fan, and H. Li, ‘Indoor Positioning Systems Based on Visible Light Communication: State of the Art’, *IEEE Commun. Surv. Tutorials*, vol. 19, no. 4, pp. 2871–2893, 2017, doi: 10.1109/COMST.2017.2743228.

[5] P. Du *et al.*, ‘Experimental Demonstration of 3D Visible Light Positioning Using Received Signal Strength With Low-Complexity Trilateration Assisted by Deep Learning Technique’, *IEEE Access*, vol. 7, pp. 93986–93997, 2019, doi: 10.1109/ACCESS.2019.2928014.

[6] T. Akiyama, M. Sugimoto, and H. Hashizume, ‘Time-of-arrival-based smartphone localization using visible light communication’, in *2017 International Conference on Indoor Positioning and Indoor Navigation (IPIN)*, Sep. 2017, pp. 1–7. doi: 10.1109/IPIN.2017.8115904.

[7] P. Du, S. Zhang, C. Chen, A. Alphones, and W.-D. Zhong, ‘Demonstration of a Low-Complexity Indoor Visible Light Positioning System Using an Enhanced TDOA Scheme’, *IEEE*

Photonics Journal*, vol. 10, no. 4, pp. 1–10, Aug. 2018, doi: 10.1109/JPHOT.2018.2841831.

[8] H. Steendam, ‘A 3-D Positioning Algorithm for AOA-Based VLP With an Aperture-Based Receiver’, *IEEE J. Select. Areas Commun.*, vol. 36, no. 1, pp. 23–33, Jan. 2018, doi: 10.1109/JSAC.2017.2774478.

[9] F. Wei, Y. Wu, S. Xu, and X. Wang, ‘Accurate visible light positioning technique using extreme learning machine and meta-heuristic algorithm’, *Optics Communications*, vol. 532, p. 129245, Apr. 2023, doi: 10.1016/j.optcom.2022.129245.

[10] Y. Yang *et al.*, ‘Positioning Using Wireless Networks: Applications, Recent Progress and Future Challenges’, 2024, *arXiv*. doi: 10.48550/ARXIV.2403.11417.

[11] Z. Zhu, Y. Yang, M. Chen, C. Guo, J. Cheng, and S. Cui, ‘A Survey on Indoor Visible Light Positioning Systems: Fundamentals, Applications, and Challenges’, 2024, *arXiv*. doi: 10.48550/ARXIV.2401.13893.

[12] Y.-C. Wu *et al.*, ‘Received-Signal-Strength (RSS) Based 3D Visible-Light-Positioning (VLP) System Using Kernel Ridge Regression Machine Learning Algorithm With Sigmoid Function Data Preprocessing Method’, *IEEE Access*, vol. 8, pp. 214269–214281, 2020, doi: 10.1109/ACCESS.2020.3041192.

[13] J. He *et al.*, ‘Demonstration of high precision 3D indoor positioning system based on two-layer ANN machine learning technique’, in *Optical Fiber Communication Conference (OFC) 2019*, San Diego, California: OSA, 2019, p. Th3I.2. doi: 10.1364/OFC.2019.Th3I.2.

[14] F. Zafari, A. Gkelias, and K. K. Leung, ‘A Survey of Indoor Localization Systems and Technologies’, *IEEE Commun. Surv. Tutorials*, vol. 21, no. 3, pp. 2568–2599, 2019, doi: 10.1109/COMST.2019.2911558.

[15] H. Liu, H. Darabi, P. Banerjee, and J. Liu, ‘Survey of Wireless Indoor Positioning Techniques and Systems’, *IEEE Trans. Syst., Man, Cybern. C*, vol. 37, no. 6, pp. 1067–1080, Nov. 2007, doi: 10.1109/TSMCC.2007.905750.

[16] K. Wang and H. Tan, ‘Positioning algorithm based on space constraint of the PD array in VLP system’, *Optics Communications*, vol. 561, p. 130510, Jun. 2024, doi: 10.1016/j.optcom.2024.130510.

[17] X. Yu, J. Wang, and H. Lu, ‘Single LED-Based Indoor Positioning System Using Multiple Photodetectors’, *IEEE Photonics J.*, vol. 10, no. 6, pp. 1–8, Dec. 2018, doi: 10.1109/JPHOT.2018.2848947.

[18] A. H. A. Bakar, T. Glass, H. Y. Tee, F. Alam, and M. Legg, ‘Accurate Visible Light Positioning Using Multiple-Photodiode Receiver and Machine Learning’, *IEEE Trans. Instrum. Meas.*, vol. 70, pp. 1–12, 2021, doi: 10.1109/TIM.2020.3024526.

[19] L.-S. Hsu *et al.*, ‘Utilizing single light-emitting-diode (LED) lamp and silicon solar-cells visible light positioning (VLP) based on angle-of-arrival (AOA) and long-short-term-memory-neural-network (LSTMNN)’, *Optics Communications*, vol. 524, p. 128761, Dec. 2022, doi: 10.1016/j.optcom.2022.128761.

[20] I. Alonso-González, D. Sánchez-Rodríguez, C. Ley-Bosch, and M. A. Quintana-Suárez, ‘Discrete Indoor Three-Dimensional Localization System Based on Neural Networks Using Visible Light Communication’, *Sensors*, vol. 18, no. 4, Art. no. 4, Apr. 2018, doi: 10.3390/s18041040.

[21] A. A. Mahmoud, Z. U. Ahmad, O. C. L. Haas, and S. Rajbhandari, ‘Precision indoor three-dimensional visible light positioning using receiver diversity and multi-layer perceptron neural network’, *IET Optoelectronics*, vol. 14, no. 6, pp. 440–446, 2020, doi: 10.1049/iet-opt.2020.0046.

[22] S. Li, L. Qin, D. Zhao, and X. Hu, ‘Indoor positioning system for single LED light based on deep residual shrinkage network’, *Optics Communications*, vol. 559, p. 130366, May 2024, doi: 10.1016/j.optcom.2024.130366.

[23] J. Li, Y. Huang, S. Huang, I. Tavakkolnia, H. Haas, and M. Safari, ‘Integrated Communication and Positioning for IRS-Assisted LiFi Networks’, in *2024 IEEE Wireless Communications and Networking Conference (WCNC)*, Dubai, United Arab Emirates: IEEE, Apr. 2024, pp. 01–06. doi: 10.1109/WCNC57260.2024.10570819.

[24] R. Wang, Y. Sun, Z. Liu, M. Gao, and X. You, ‘Integrated Mobile Visible Light Communication and Positioning Systems Based on Decision Feedback Channel Estimation’, *Photonics*, vol. 11, no. 6, p. 537, Jun. 2024, doi: 10.3390/photonics11060537.

[25] S. Rajbhandari *et al.*, ‘A review of gallium nitride LEDs for multi-gigabit-per-second visible light data communications’, *Semiconductor Science and Technology*, vol. 32, no. 2, p. 023001, Feb. 2017, doi: 10.1088/1361-6641/32/2/023001.

[26] L. Zeng *et al.*, ‘High data rate multiple input multiple output (MIMO) optical wireless communications using white led lighting’, *IEEE J. Select. Areas Commun.*, vol. 27, no. 9, pp. 1654–1662, Dec. 2009, doi: 10.1109/JSAC.2009.091215.

[27] A. H. Azhar, T.-A. Tran, and D. O’Brien, ‘A Gigabit/s Indoor Wireless Transmission Using MIMO-OFDM Visible-Light Communications’, *IEEE Photon. Technol. Lett.*, vol. 25, no. 2, pp. 171–174, Jan. 2013, doi: 10.1109/LPT.2012.2231857.

[28] K. Werfli *et al.*, ‘Experimental Demonstration of High-Speed 4 × 4 Imaging Multi-CAP MIMO Visible Light Communications’, *J. Lightwave Technol.*, vol. 36, no. 10, pp. 1944–1951, May 2018, doi: 10.1109/JLT.2018.2796503.

[29] M. Dehghani Soltani *et al.*, ‘High-Speed Imaging Receiver Design for 6G Optical Wireless Communications: A Rate-FOV Trade-Off’, *IEEE Trans. Commun.*, vol. 71, no. 2, pp. 1024–1043, Feb. 2023, doi: 10.1109/TCOMM.2022.3230954.

[30] D. E. Rumelhart, G. E. Hinton, and R. J. Williams, ‘Learning representations by back-propagating errors’, *Nature*, vol. 323, no. 6088, pp. 533–536, Oct. 1986, doi: 10.1038/323533a0.

[31] M. T. Hagan and M. B. Menhaj, ‘Training feedforward networks with the Marquardt algorithm’, *IEEE Trans. Neural Netw.*, vol. 5, no. 6, pp. 989–993, Nov. 1994, doi: 10.1109/72.329697.